Evolution of Magnetic Fields and Energy Release Processes during Homologous Eruptive Flares

Suraj Sahu[1,2], Bhuwan Joshi[1], Avijeet Prasad[3,4], and Kyung-Suk Cho[5,6]

[1] Udaipur Solar Observatory, Physical Research Laboratory, Dewali, Badi Road, Udaipur-313 001, Rajasthan, India; suraj@prl.res.in, sahusuraj419@gmail.com
[2] Discipline of Physics, Indian Institute of Technology Gandhinagar, Palaj, Gandhinagar-382 355, Gujarat, India
[3] Rosseland Centre for Solar Physics, University of Oslo, Postboks 1029, Blindern NO-0315, Oslo, Norway
[4] Institute of Theoretical Astrophysics, University of Oslo, Postboks 1029, Blindern NO-0315, Oslo, Norway
[5] Space Science Division, Korea Astronomy and Space Science Institute, Daejeon 305-348, Republic of Korea
[6] Department of Astronomy and Space Science, University of Science and Technology, Daejeon 305-348, Republic of Korea

Abstract

We explore the processes of the repetitive buildup and the explosive release of magnetic energy, together with the formation of magnetic flux ropes, which eventually resulted in three homologous eruptive flares of successively increasing intensities (i.e., M2.0, M2.6, and X1.0). The flares originated from NOAA active region 12017 between 2014 March 28 and 29. EUV observations and magnetogram measurements, together with coronal magnetic field modeling, suggest that the flares were triggered by the eruption of flux ropes that were embedded in a densely packed system of loops within a small part of the active region. In X-rays, the first and second events show similar evolutions, with single compact sources, while the third event exhibits multiple emission centroids, with a set of strong nonthermal conjugate sources at 50–100 keV during the hard X-ray peak. Over an interval of $\approx$ 44 hr, the photospheric magnetic field encompassing the three flares undergoes important phases of emergence and cancellation, together with significant changes near the polarity inversion lines within the flaring region. Our observations point toward the tether-cutting mechanism being the plausible triggering process of the eruptions. Between the second and third events, we observe a prominent phase of flux emergence that temporally correlates with the buildup phase of free magnetic energy in the active region corona. In conclusion, our analysis reveals efficient coupling between the rapidly evolving photospheric and coronal magnetic fields in the active region, leading to a continued phase of the buildup of free energy, which results in the homologous flares of successively increasing intensities.

1. Introduction

Solar flares are sudden explosive events in the solar atmosphere that release huge amounts of energy, in the form of heat, radiation, and bulk plasma motion, and produce highly accelerated charged particles (Fletcher et al. 2011; Benz 2017). It is widely believed that the fundamental processes that drive an eruptive event—the buildup/storage of free magnetic energy and its explosive release via magnetic reconnection—are inherently guided by the complexity of the solar magnetic fields (Priest & Forbes 2002). Therefore, in order to understand the drivers of solar flares and their associated processes, it is important to analyze the variability in the buildup and release of magnetic energy. Solar eruptive phenomena involve the expulsion of magnetized plasma out into the heliosphere. Hence, in order to understand the dynamics of the magnetized plasma during and after the explosive energy release, we need to explore multiwavelength and multi-instrument data, together with coronal magnetic field modeling.

The regions of the Sun with the strongest magnetic fields are known as solar active regions (ARs). These ARs present diverse natures in terms of their morphology, depending upon

the distribution and strength of the underlying photospheric magnetic fields (Toriumi & Wang 2019). Typically, during the growth phase, as an AR expands and evolves, the complexity of the photospheric magnetic fields increases. A complex AR may produce several energetic events—such as flares, coronal mass ejections (CMEs), jets, prominence eruptions, etc.—over its whole lifetime (Joshi et al. 2018; Mitra et al. 2018, 2020b; Sahu et al. 2020; Zuccarello et al. 2021).

Solar eruptions may originate in a repetitive manner from the same location of the AR, and sometimes they can show morphological resemblances in their multiwavelength imaging and coronagraphic observations. Such repetitive activities are known as "homologous eruptions" (Woodgate et al. 1984; Zhang & Wang 2002). Exploring homologous eruptions is extremely important for understanding the role of the photospheric magnetic field variations and associated coronal changes in determining the eruptivity. In this way, by assessing the homology tendency of an AR, we can provide important inputs for understanding the onset of CMEs and subsequent space weather consequences. In the past, several studies of different features of homologous eruptions have been carried out, revealing the following aspects to be responsible for the occurrence of homologous activity: flux emergence (Nitta & Hudson 2001; Chatterjee & Fan 2013), shearing motions and magnetic flux cancellation (Li et al. 2010; Vemareddy 2017), the persistent photospheric horizontal motion of the magnetic

structure along the polarity inversion line (PIL; Romano et al. 2015, 2018), and the coronal null point configuration (DeVore & Antiochos 2008), among others. Homologous solar eruptions form a contemporary topic of research in solar physics, and the present study aims to provide additional observational inputs in this direction.

In this study, we present detailed evolutions of the photospheric magnetic fields that were associated with three homologous eruptive flares that occurred between 2014 March 28 and 29 in the NOAA AR 12017. Interestingly, these three homologous events are of successively increasing intensities (M2.0, M2.6, and X1.0). In our previous study (Sahu et al. 2022), we explored the formation processes of three homologous broad CMEs that resulted from these three eruptive flares. We have identified the events as flux rope eruptions originating from the same compact flaring region (FR) of the AR. Our work has presented a clear example of a large-scale coronal magnetic configuration that has been repeatedly blown out by compact flux rope eruptions, leading to a series of broad CMEs. The flaring activities in AR 12017, especially the X-class event on 2014 March 29, have been subjected to various studies involving observational and modeling analyses (Kleint et al. 2015; Li et al. 2015; Liu et al. 2015; Young et al. 2015; Yang et al. 2016; Woods et al. 2017, 2018; Cheung et al. 2019). Liu et al. (2015) discussed a scenario of asymmetric filament eruption, in the context of nonuniform filament confinement and an MHD instability prior to the X-flare. The study by Yang et al. (2016) comprised all the flaring activities in the AR between 2014 March 28 and 29. They concluded that the flares were mainly triggered by the kink instability of the associated filaments. Woods et al. (2018) investigated the triggering mechanism of the third event (the X1.0 flare) and the associated filament eruption. Their study confirmed the existence of two flux ropes within the AR prior to the flaring. Interestingly, one of these two flux ropes erupted, which may have been due to the tether-cutting reconnection (Moore et al. 2001), allowing the flux rope to rise to a torus unstable region. In this paper, our motivation is to conduct a detailed study in order to understand the repetitive buildup of magnetic energy and flux ropes that eventually drive the three homologous eruptive flares. Toward this, we provide a quantitative estimation of the temporal evolution of the free magnetic energy in the AR, and we examine precisely the changes in photospheric magnetic flux over the entire period of the homologous flaring activity. We further present a detailed multiwavelength investigation of the temporal, spatial, and spectral characteristics of each event. In Section 2, we provide a brief discussion of the data sources and analysis techniques. Section 3 gives the details of the EUV and X-ray observations of the flares. In Section 4, we describe the evolutions of the photospheric magnetic fields during the events, as well as the associated coronal magnetic configuration. The buildup of the photospheric current in relation to the triggering of the eruptions is presented in Section 5. The evolutionary stages of the eruptive hot plasma structures are presented in Section 6. The details of the storage and release processes of the free magnetic energy are described in Section 7. We discuss and interpret our results in the final section.

2. Observational Data Sources and Techniques

We use data from the Atmospheric Imaging Assembly (AIA; Lemen et al. 2012) on board the Solar Dynamics Observatory

Table 1
The Flares in NOAA AR 12017 between 2014 March 28 and 29

Flare	Flare Class	Date	Time (UT)		
			Start	Peak	End
F1	M2.0	2014 March 28	19:05	19:18	19:27
F2	M2.6	2014 March 28	23:44	23:51	23:58
F3	X1.0	2014 March 29	17:35	17:48	17:54

(SDO; Pesnell et al. 2012) for EUV imaging and analysis. AIA observes the full disk of the Sun in seven EUV (94 Å, 131 Å, 171 Å, 193 Å, 211 Å, 304 Å, and 335 Å), two UV (1600 Å and 1700 Å), and one visible (4500 Å) channels. For our analysis, we use the EUV 304 Å [$\log(T) \approx 4.7$] and 193 Å [$\log(T) \approx 6.2$, 7.3] observations. The 304 Å images provide information about the chromosphere and transition region of the Sun, while the 193 Å images are used to analyze the corona and hot flare plasma. In order to investigate the evolution of the photosphere through line-of-sight (LOS) magnetogram and continuum observations, we obtain data from the Helioseismic Magnetic Imager (HMI; Schou et al. 2012) on board the SDO.

To visualize the X-ray sources and to quantify the parameters that are associated with the X-ray emission processes, we use data obtained from the Reuven Ramaty High Energy Solar Spectroscopic Imager (RHESSI; Lin et al. 2002). RHESSI observes full-disk solar X-ray sources in the energy range of 3 keV to 17 MeV. We use the CLEAN algorithm (Hurford et al. 2002) to reconstruct the X-ray images in different energy bands (i.e., 3–6, 6–12, 12–25, 25–50, and 50–100 keV). For image reconstruction, we use the front segments of detectors 3–8, with a 20 s integration time. We also carry out X-ray spectroscopy using the RHESSI data. The details of the spectroscopy are given in Section 3.3.

For the calculation of the free magnetic energy associated with the AR in the coronal volume, we need 3D information about the magnetic field above the photosphere. For this purpose, we use the nonlinear force-free field (NLFFF) extrapolation technique, which was originally formulated by Wiegelmann (2008), then further developed by Wiegelmann & Inhester (2010) and Wiegelmann et al. (2012). We use the vector magnetograms (HMI.sharp_cea_720s series) as the photospheric input boundary conditions for the extrapolation. The extrapolation volume extends up to 280, 229, and 183 Mm in the X, Y, and Z directions, respectively, considering the photosphere as the X–Y plane.

3. Multiwavelength Analysis of Flare Evolution

3.1. Multiwavelength Overview of AR 12017

Our study focuses on three homologous flaring events of successively increasing intensities (M2.0, M2.6, and X1.0). The flares occurred in NOAA AR 12017 between 2014 March 28 and 29. A summary of the flares is given in Table 1, which is based on the GOES flare catalog.[7] The three flares are indicated along with the GOES light curves (in the 1–8 and 0.5–4 Å channels) in Figure 1. The durations of the three flares are marked by the vertical pink stripes. The gray shaded region indicates an interval, when the GOES data were unavailable.
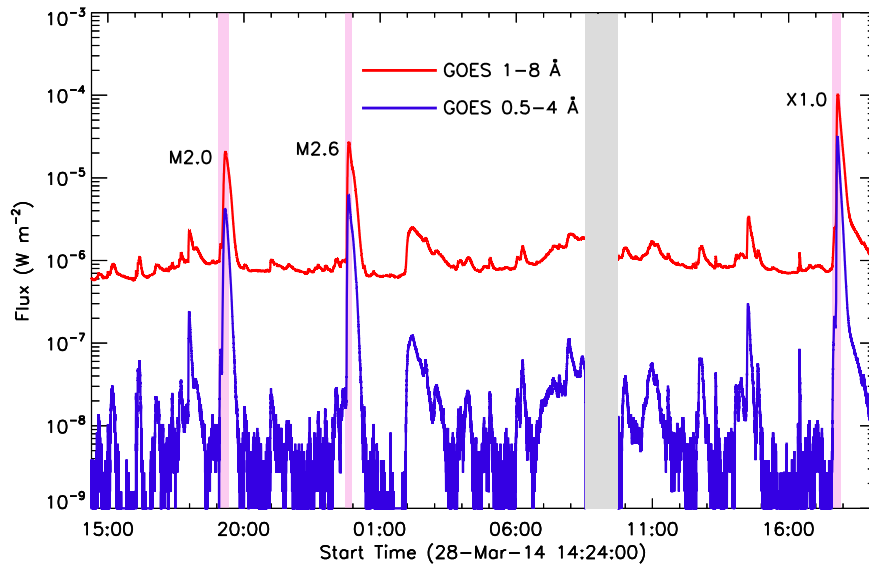
Figure 1. GOES light curves in the 1–8 and 0.5–4 Å channels, showing the three flares (M2.0, M2.6, and X1.0) under analysis. The intervals of the three flares are shown by the pink vertical stripes. The gray shaded region indicates an interval when the GOES data were unavailable.

In Figure 2, we provide a multiwavelength view of AR 12017, by plotting simultaneous white-light continuum, magnetogram, and EUV images, prior to the onset of the first event of M2.0 intensity. By comparing the different panels of Figure 2, one can note many interesting features of the AR and the FR. A comparison of the continuum and magnetogram images (Figures 2(a) and (b)) suggests that the leading part of the AR consists of sunspots of predominantly negative polarity (see the regions enclosed by the boxes in the various panels of Figure 2), which happen to be the source of the eruptive flares under analysis. Hence, we term the region inside the box the FR. On the trailing part of the AR, we observe sparsely located small sunspots with dispersed fluxes of predominantly positive polarity (Figures 2(a) and (b)). The EUV images at 171 and 193 Å readily suggest the existence of large coronal loops connecting the leading and trailing parts of the AR (Figures 2(c) and (d)). The presence of a compact closed-loop configuration in the FR is also clearly visible. In Figure 2(e), we provide a preflare 304 Å image of AR 12017. Here, we can clearly distinguish the dominance of the brighter emission from the FR over the other parts of the AR.

3.2. Temporal and Spatial Aspects

The temporal and spatial evolutions in the EUV 304 Å observations of the M2.0 (F1), M2.6 (F2), and X1.0 (F3) flares are presented in Figures 3, 5, and 6, respectively. In all these figures, panel (a) presents the light curves of the flares, while panels (b)–(g) show their spatial evolutions. The temporal evolutions of the flares have been studied with GOES 1–8 Å, AIA 304 Å, and RHESSI X-ray light curves. We have reconstructed the RHESSI X-ray light curves in various energy bands, viz, 3–6, 6–12, 12–25, 25–50, and 50–100 keV. For F1, we do not show the 50–100 keV light curve, due to the lack of significant X-ray flux above 50 keV. To explore the spatial structures in the FRs and their evolutions at the upper chromospheric level, we plot a few representative AIA 304 Å images, which are overplotted by the RHESSI X-ray sources at various energy bands. We note that the X-ray emission sources at 6–12 keV are exactly cospatial with the lower-energy

sources at 3–6 keV, hence they are not shown in these figures. To understand the evolutions of the spatial structures at the flaring corona, we show the EUV 193 Å images in Figures 4(a) to (d) and (e) to (h) and Figure 7 for F1, F2, and F3, respectively.

3.2.1. M2.0 Flare

Before the beginning of the rise phase of F1, we observe a preflare enhancement in the X-ray light curves at ≈19:08 UT. We note that this preflare hump is absent from the AIA 304 Å light curve, which exclusively represents emission from the FR. This observation suggests that this preflare emission is not associated with the flaring event under analysis. We observe plasma eruption from the eastern part of the FR in the form of a collimated stream (as indicated by the arrows in Figures 3(b) and (c)) at the outset of F1 (see the animation attached to Figure 3). At the base of the collimated structure, we note X-ray emission up to 25 keV, as shown by the contours of the different energy bands. During the peak of the flare (≈19:18 UT), the hard X-ray (HXR) source of 25–50 keV appears at the flaring core (shown by the black contours in Figure 3(d)). After the flare's peak, we observe the eruption of cool (i.e., dark) plasma from the western part of the core region (shown by the arrows in Figures 3(e) and (g); see also the attached animation). During this period, the X-ray sources up to 25 keV are observed as a single source, suggesting X-ray production from a compact and dense system of coronal loops. The X-ray sources in the decay phase (Figures 3(f) and (g)) further confirm this scenario, as the X-ray emission is observed to originate above the closely packed postflare loop system.

The evolutionary stages of F1 in the EUV 193 Å images are shown in Figures 4(a) and (d). Prior to the flare, we detect an activated filament (indicated by the arrow in Figure 4(a)), with a clear signature of activity in the form of the brightening at its base. Subsequently, the filament erupts in a jet-like manner (marked by the arrow in Figure 4(b)), with a morphological similarity to the collimated stream observed in the EUV 304 Å images (see Figures 3(b) and (c)). The start of the impulsive rise phase of the flare can be discerned in the form of the extended brightening over
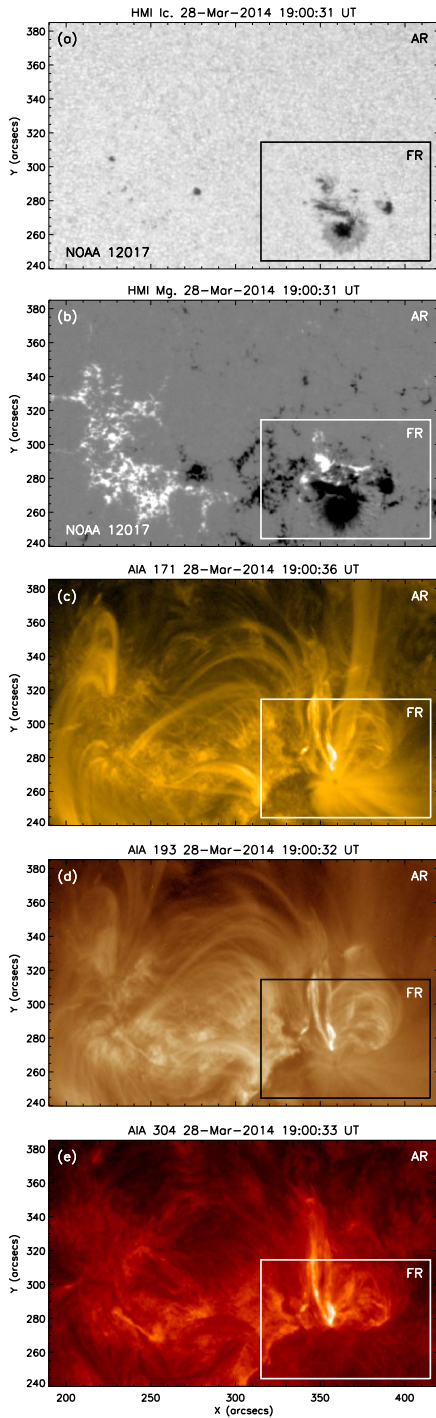
3

Figure 2. Multiwavelength view of AR 12017 on 2014 March 28 at ≈ 19:00 UT (i.e., 5 minutes before the start of the first flare, according to the GOES data). (a) HMI continuum image of the AR. We observe a large sunspot in the leading part of the AR, which we mark with the black box. The flares in our study occurred within this marked area of the AR, which we term the FR. We indicate the FR with the boxes in all the subsequent panels. (b) HMI LOS magnetogram of the AR. The FR consists of a strong negative-polarity region, together with relatively weaker compact positive polarities, which are located north of it. (c) and (d) AIA 171 Å [log(T) ≈ 5.7] and 193 Å [log(T) ≈ 6.2, 7.3] images showing the connectivity of the different loop systems between the leading and trailing parts of the AR, along with compact loops within the FR. (e) AIA 304 Å [log(T) ≈ 4.7] image displaying the much brighter emission from the FR in comparison to the other parts of the AR.

the FR (Figure 4(c); see also Figure 3(a)). Afterward, we observe the formation of compact postflare loop arcades in the core region (shown by the arrow in Figure 4(d)).

3.2.2. M2.6 Flare

The evolutionary stages of F2 are shown in Figure 5 through the EUV 304 Å image sequences. As with F1, in this case we also observe a single X-ray source throughout the flare evolution. Furthermore, the X-ray sources from lower to higher energies (e.g., 6–12, 12–25, 25–50, and 50–100 keV) are observed to be cospatial. During the peak of the flare (≈ 23:50 UT), the X-ray sources in the energy band of 50–100 keV are observed to appear in the core region (Figure 5(d)). Thereafter, the 50–100 keV source disappears, while the X-ray emission in the lower-energy bands persists (Figures 5(e) and (g)). We note a double-peak structure in the AIA 304 Å light curve during the peak time of the flare (see Figure 5(a)). This double-peak structure suggests two successive episodes of intense brightening, which accompany the eruptions from the eastern and western parts of the FR, respectively (indicated by the arrows in Figures 5(c) and (d); see also the animation attached to Figure 5), which ultimately result in the flaring intensity of the M2.6 class. Notably, the eruptions in this case are not jet-like ejections, as in the case of F1.

In Figures 4(e) to (h), we show the EUV 193 Å images that present the evolutionary stages of F2. Prior to the flare, we observe a bright activated loop system in the core region (indicated by the arrow in Figure 4(e)). This loop structure subsequently erupts (marked by the arrow in Figure 4(f)) in a nearly coherent manner, which also marks the beginning of the impulsive phase of the flare (see Figure 5(a)). Thereafter, the erupting loop system loses its coherency, and we use an arrow to mark its bright eastern part in Figure 4(g). Later on, dense and compact postflare loop arcades are observed to form in the core region (indicated by the arrow in Figure 4(h)).

3.2.3. X1.0 Flare

The evolution of the X1.0 flare (F3) is shown by a few representative AIA 304 Å images in Figures 6(b) to (g). Prior to the impulsive phase of the event, starting at ≈ 17:44 UT, we observe a clear signature of preflare activity persisting for ≈8 minutes (≈17:36–17:44 UT). This preflare phase is discernible in all the X-ray and EUV light curves (Figure 6(a)), and the preflare activity is observed in the AIA images as enhanced brightening, from the western part of the core region, which also emits X-ray sources up to 25 keV (Figures 6(b) and (c)). Thereafter, the X-ray sources evolve at two separate locations, and we observe emission up to 25 keV from both the eastern and western parts of the flaring core region (Figure 6(d)). The X-ray emission in the 6–12 keV energy range persists in the eastern part of the core, whereas the strong emission in the energy range of 25–50 keV is observed as appearing in the western part of the flaring core (Figure 6(e)). During the peak of the HXR light curves, we observe clear X-ray sources in the 50–100 keV energy band. Importantly, this high-energy source presents an elongated structure with two distinct centroids (Figure 6(f)). Subsequently, the X-ray emission up to 50 keV persists, which is observed as a single-source structure in multiple energy bands (Figure 6(g)).
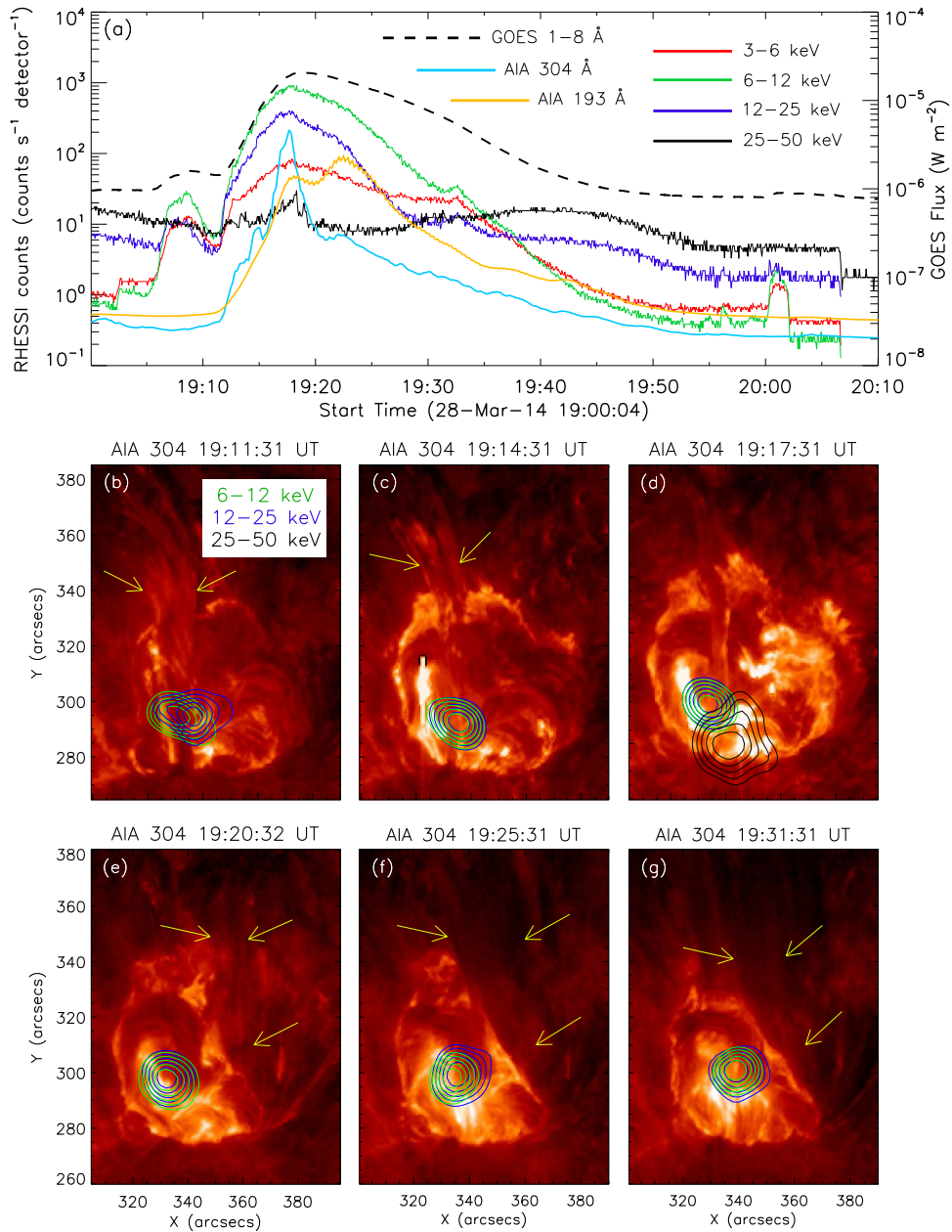
Figure 3. (a) RHESSI X-ray count rates in different energy bands between 3 and 50 keV during the M2.0 event. The GOES flux profile in the 1–8 Å channel and the AIA 193 and 304 Å light curves of the FR are also overplotted. (b)–(g) The evolution of the flare, as shown in AIA 304 Å images. The X-ray contours in 6–12, 12–25, and 25–50 keV are overplotted on the EUV images. The X-ray images are reconstructed by the CLEAN algorithm, with an integration time of 20 s. The contours are drawn at 50%, 60%, 70%, 80%, and 90% of the peak flux in each image. The yellow arrows—except in (d)—indicate the plasma eruptions originating from the core region. An animation is associated with this figure, showing the evolutionary stages of the flare in the AIA 304 Å observations.

(An animation of this figure is available.)

The evolution of F3 in the EUV 193 Å images is presented in Figure 7. Similar to the EUV 304 Å observations, in these images we also observe a clear signature of enhanced brightening, from the western part of the core, revealing the preflare activity (indicated by the arrows in Figures 7(a) and (b)). Subsequently, this preflare enhancement spreads over the whole core region (Figures 7(c) and (d)). During the main phase of the flare, intense widespread flare emissions are observed from the core (Figures 7(e) and (f)). Thereafter, the postflare loop arcades are observed to form (shown by the arrow in Figure 7(g)), which gradually get denser and brighter,

before they are observed extending over a large area of the core (marked by the arrow in Figure 7(h)).

3.3. RHESSI X-Ray Spectroscopy

To quantify the thermal and nonthermal components of the X-ray emission during these three flares, we conduct X-ray spectroscopic analysis using RHESSI observations. We generate RHESSI spectra with an energy binning of $1/3$ keV from 6 to 15 keV, 1 keV from 15 to 100 keV, and 5 keV from 100 keV onward. We use the front segments of detectors 1–9 (except for detectors 2 and 7, which have a lower energy
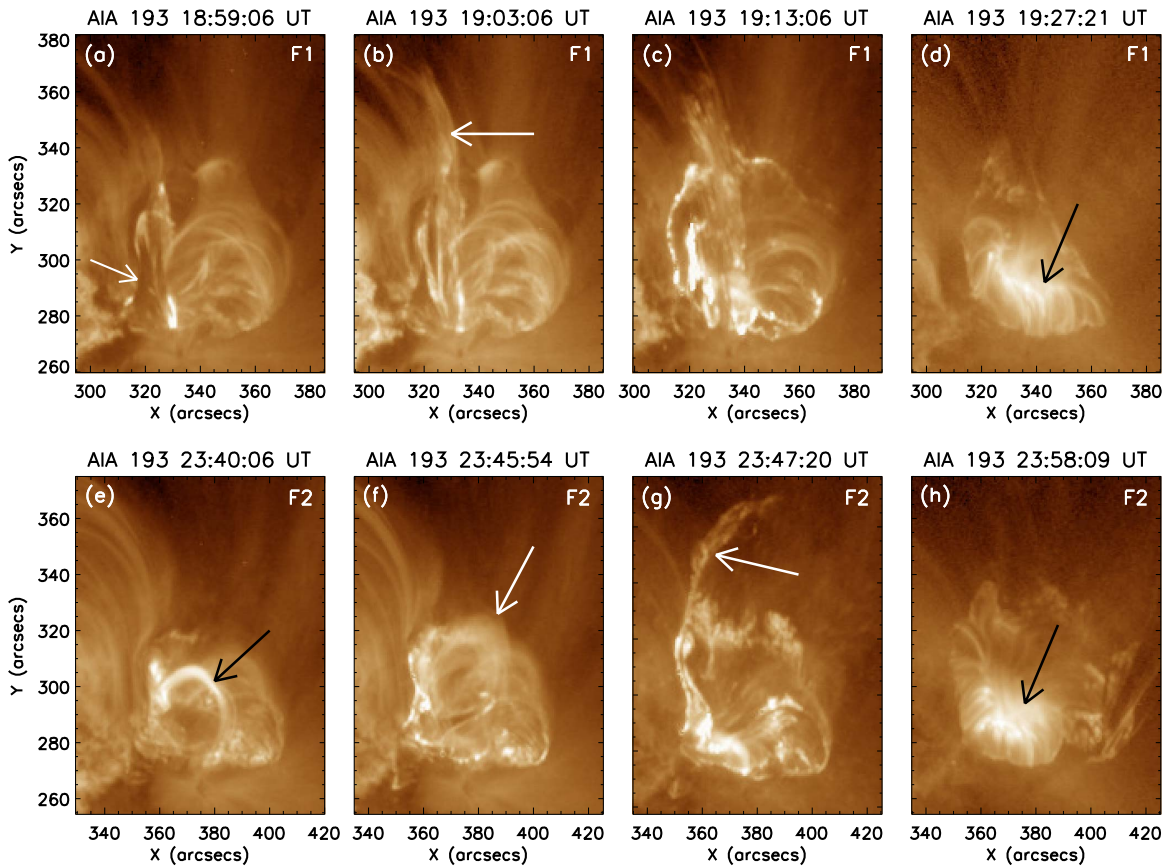
Figure 4. (a)–(d) The evolution of the M2.0 flare (F1) in the AIA 193 Å images. In (a), we use an arrow to indicate an activated filament with clear brightening at its base. (b) The subsequent jet-like eruption of the filament. (c) The extended brightening within the FR, which marks the start of the impulsive phase of the flare. In (d), we use an arrow to indicate the compact postflare loop system. (e)–(h) The evolution of the M2.6 flare (F2) in the AIA 193 Å images. In (e), we use an arrow to mark a bright loop system in the core region observed prior to the flare. This loop system subsequently erupts in a coherent manner, which we indicate with the arrow in (f). Thereafter, the erupting structure evolves noncoherently. We use an arrow to mark the bright eastern part of the erupting structure in (g). In (h), we use an arrow to indicate the compact bright postflare loop arcades.

resolution and a higher threshold energy, respectively). The spectra are deconvolved with the full detector response matrix (i.e., offdiagonal elements are included; Smith et al. 2002). For the thermal fitting, we use an isothermal model constructed using the line spectrum. The nonthermal spectra are fitted using the thick-target bremsstrahlung model (Holman et al. 2003). We derive the temperature (T) and the emission measure (EM) of the hot flaring plasma from the thermal fit, and we derive the electron spectral index (δ) from the nonthermal component.

The results obtained from the spectral fit of the X-ray emission from the FR are presented in Figures 8(a), (b), and (c), for F1, F2, and F3, respectively. For F1, the GOES flare peak ($\approx$ 19:18 UT on 2014 March 28) coincides with the HXR (25–50 keV) peak. A high value of the electron spectral index (i.e., $\delta = 8.7$) indicates a mild nonthermal component of the flaring X-ray emission. During the F2 peak, the electron spectral index decreases to 3.3, indicating a much harder nonthermal spectrum compared to F1. From the thermal spectral fit, we obtain the temperature of the FR as $\approx$25.6 MK, which is higher than the temperature ($\approx$20.9 MK) during the peak of F1. During F3, the hardness of the spectrum remains almost the same as that of F2. However, the EM ($\approx$61 $\times$ 10^{47} cm^{-3}) increases by an order of magnitude during F3, as compared to the previous two events (see Figures 8(a) to (c)). This indicates a significant enhancement in the electron density of the hot ($T \approx 26$ MK) plasma within the flaring volume.

4. Structure and Evolution of Magnetic Fields

4.1. Photospheric Magnetic Fields

We analyze the structural and temporal evolutions of the photospheric magnetic fields of the FR in Figure 9. To examine the magnetic flux changes quantitatively, we plot spatial variations of the positive and negative magnetic flux of the region of interest (shown in Figures 9(b) to (m)). In Figure 9(a), we provide the time profiles of the integrated magnetic fluxes through the selected area (see Figures 9(b) to (m)), together with the GOES 1–8 Å soft X-ray (SXR) light curve. The time profiles of the magnetic fluxes are for the period from 00:00 UT on 2014 March 28 to 20:00 UT on 2014 March 29 ($\approx$44 hr), covering all the flare events under analysis. Also, the chosen interval includes a time span of $\approx$19 hr before F1, to examine the buildup of the preflare photospheric flux in detail.

In Figure 9(a), we select six different epochs ($t1$, $t2$, $t3$, $t4$, $t5$, and $t6$) to explore the spatial changes in the photospheric magnetic field distribution. Among these epochs $t3$, $t4$, and $t6$ are selected at the peak time of the flares under analysis. The continuum and LOS magnetogram images during the epochs ($t1$–$t6$) are presented in Figures 9(b)–(m). We observe substantial structural changes in the photospheric magnetic field of the FR over the selected interval of $\approx$44 hr (see Figures 9(b)–(m) and the attached animation).
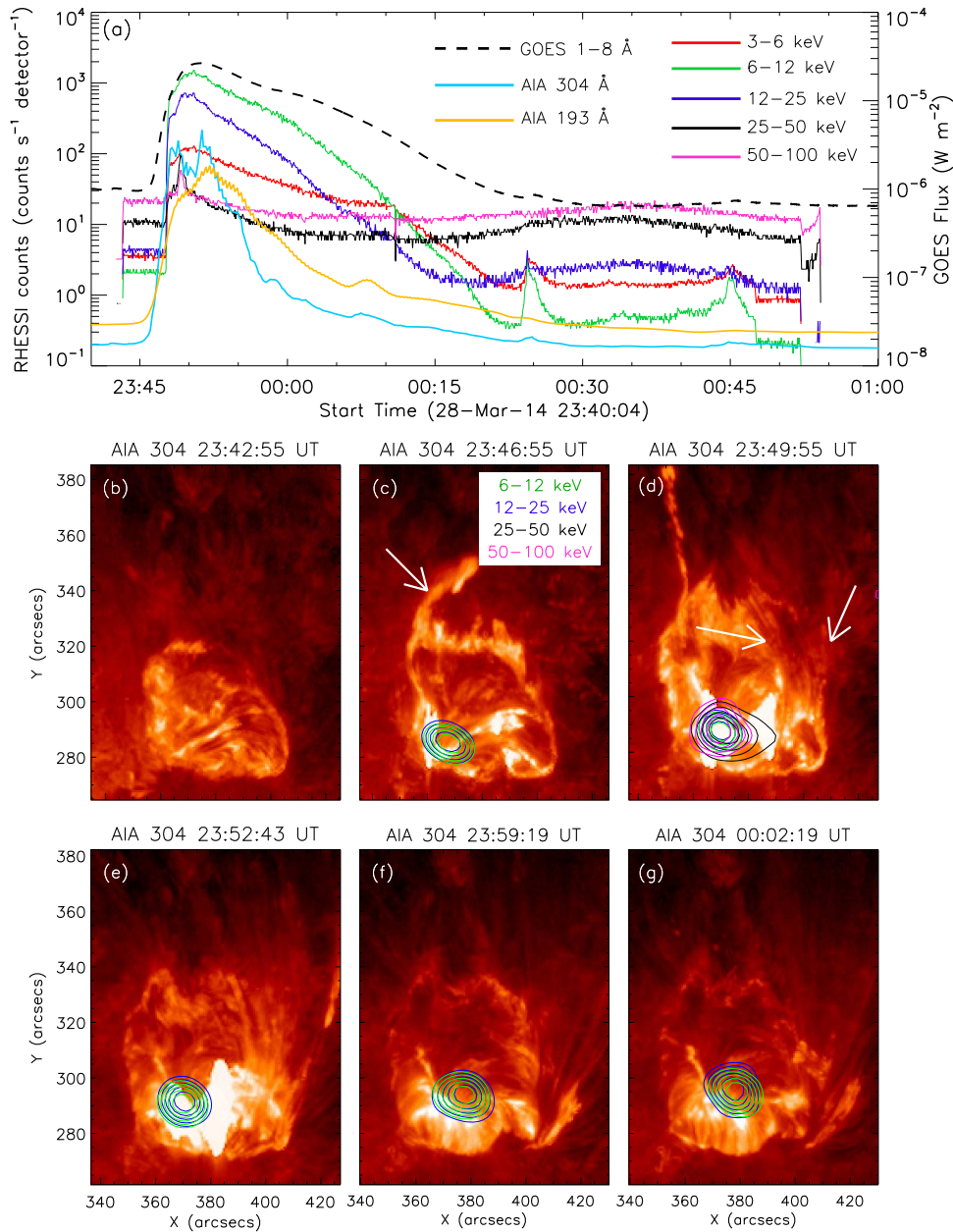
Figure 5. (a) RHESSI X-ray count rates in different energy bands between 3 and 100 keV during the M2.6 event. The GOES flux profile in the 1–8 Å channel and the AIA 193 and 304 Å light curves of the FR are also overplotted, for comparison with the X-ray light curves. (b) The preflare configuration of the FR observed in AIA 304 Å, devoid of significant X-ray emissions. (c)–(g) The evolution of the flare in the AIA 304 Å observations, with the RHESSI X-ray sources overplotted on the EUV images. In (c)–(d), we indicate the plasma structures erupting from the eastern and western parts of the FR, respectively. The X-ray contours in 6–12, 12–25, 25–50, and 50–100 keV are overplotted on the EUV images. The X-ray images are reconstructed by the CLEAN algorithm, with an integration time of 20 s. The contours are drawn at 50%, 60%, 70%, 80%, and 90% of the peak flux in each image. An animation of this figure is available, which shows the various phases of the flare in the AIA 304 Å observations.

(An animation of this figure is available.)

In Figures 9(b) to (g), we show the evolution of the FR using cotemporal continuum and magnetogram observations for three epochs—$t1$, $t2$, and $t3$—that present magnetic field changes prior to F1. The inspection of these images reveals an increase followed by a decrease of the sunspot area of the northern sunspot group (shown by the black arrows in Figures 9(b) to (d)). We also observe the growth of the compact sunspot groups on the western side of the main sunspot group (indicated by the dark blue arrows in Figures 9(b) to (d)). Figures 9(e) to (g) show cotemporal LOS magnetogram observations corresponding to the continuum images in

Figures 9(b) to (d). In Figures 9(e) and (g), we focus on the eastern and western PILs, marked by the red and sky blue dotted lines, respectively. The yellow arrows indicate the gradual decrease of the positive flux near the eastern PIL (Figures 9(e) to (g)), whereas the red arrows indicate the subsequent decrease of the negative flux (see Figures 9(g) and (k)). We further note that the orientation of the western PIL has changed from $t1$ to $t3$ (see the sky blue dotted lines in Figures 9(e) and (g)).

In Figures 9(h) to (m), we present the continuum and LOS magnetogram observations showing the evolution of the FR
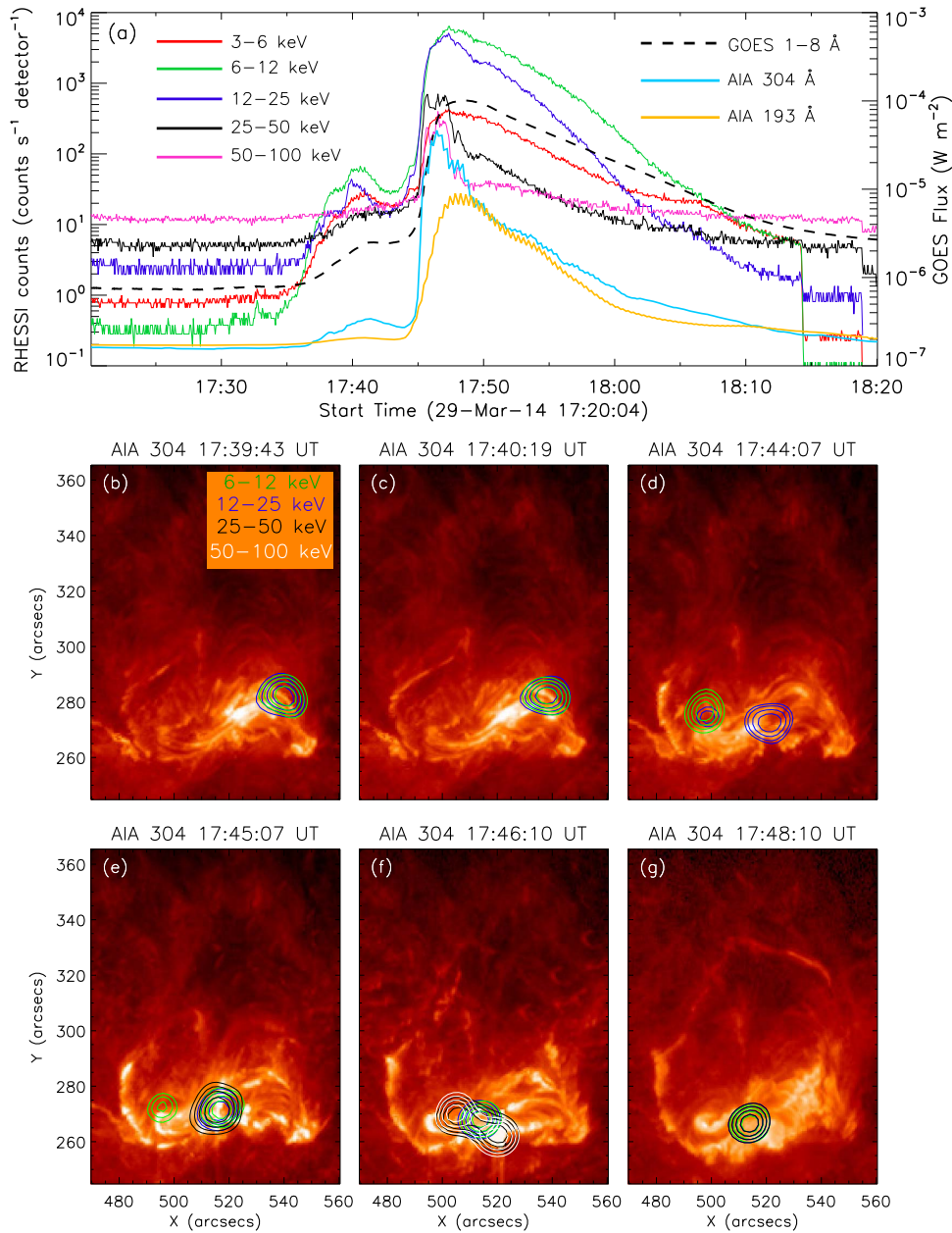
Figure 6. (a) RHESSI X-ray count rates in different energy bands between 3 and 100 keV during the X1.0 event. The GOES flux profile in the 1–8 Å channel and the AIA 193 and 304 Å light curves of the FR are overplotted. (b)–(g) AIA 304 Å observations, showing the evolution of the flare. The X-ray contours in 6–12, 12–25, 25–50, and 50–100 keV are overplotted on the EUV images. The X-ray images are reconstructed by the CLEAN algorithm, with an integration time of 20 s. The contours are drawn at 60%, 70%, 80%, and 90% of the peak flux in each image. An animation is associated with this figure, showing the different evolutionary stages of the flare in the AIA 304 Å observations.

(An animation of this figure is available.)

during epochs t4, t5, and t6, which are used to explore the changes in the photospheric magnetic field structures that are associated with F2 and F3. Notably, after F2, the photospheric configurations of the sunspot groups and associated magnetic fields in the northern region exhibit striking changes (see Figures 9(h) and (j); see also the attached animation). During the interval between F2 and F3, we observe that the northern sunspot group, with a relatively compact configuration, undergoes a rapid expansion, resulting in its fragmentation into three distinct parts (indicated by the arrows in Figure 9(j)). The magnetogram images that are cotemporal with the continuum observations are shown in Figures 9(k) to (m). The eastern and western PILs are indicated by the red and sky blue dotted lines,

respectively, in Figure 9(k). We observe clear features of flux cancellation and emergence. The sky blue arrows indicate the substantial cancellation of the negative flux near the western PIL, whereas the green arrows indicate the gradual increase of the positive flux near the same PIL. These observations showing the flux emergence and cancellation are in agreement with the qualitative estimation shown in Figure 9(a).

4.2. Magnetic Configuration of Flaring Corona

In Figure 10, we represent the preflare coronal magnetic structures in and around the FR, obtained through NLFFF extrapolation. The first, second, and third columns denote the
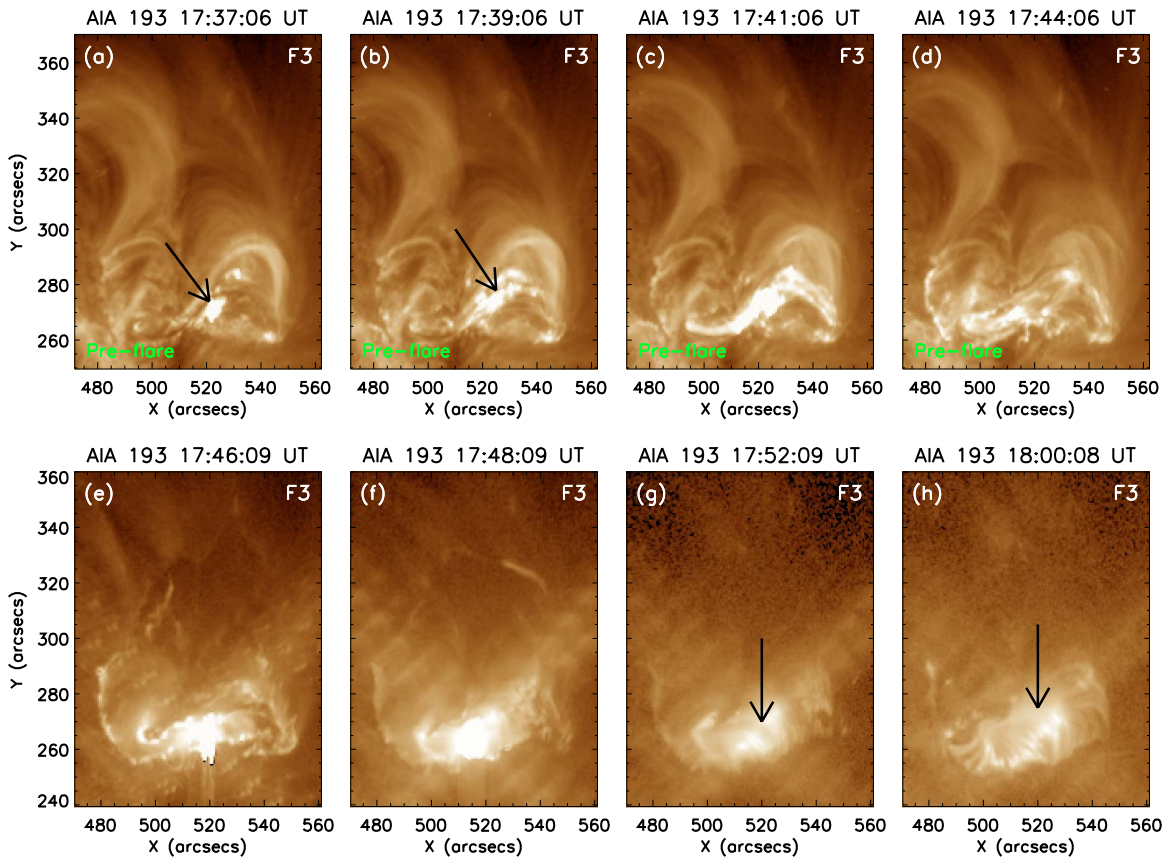
Figure 7. The evolution of the X1.0 flare (F3) in the AIA 193 Å images. (a)–(d) The morphological changes during the preflare phase of the flare. (e)–(h) The main phase of the flare. We note preflare activity, in the form of intense brightening from the western part of the core, which we indicate with the arrows in (a) and (b). This preflare intensity enhancement subsequently spreads over a large area within the core region ((c) and (d)). During the main phase of the flare, enhanced intensity is observed from an extended part of the core region ((e) and (f)). Afterward, dense postflare loop arcades are observed to form, which gradually elongate over a broad area of the core, as indicated by the arrows in (g) and (h).

epochs corresponding to F1, F2, and F3, respectively. In the top panels, we show the extrapolated coronal field lines, taking the HMI SHARP CEA radial magnetic fields as the background, whereas in the bottom panels, we show the AIA 304 Å images in the background, using the visualization software VAPOR (Li et al. 2019). In all cases, we find the existence of two flux ropes lying over the compact eastern and western PILs of the FR (see Figure 9), shown by yellow and blue field lines, respectively. The flux ropes are encompassed by the low-lying bipolar field lines (shown in green). The sequential eruptions of the flux ropes and the neighboring core field give rise to the eruptive flares under analysis. We observe filaments in the AIA 304 Å images, which are indicated by the arrows in the bottom panels. A detailed investigation into the modeling of the coronal magnetic fields during the three events is in progress, and will be presented in a subsequent study.

5. Morphology and Evolution of Photospheric Longitudinal Currents

We show the morphological changes associated with the photospheric longitudinal current in response to the magnetic field changes in Figure 11. In the photosphere, the vertical component of the electric current density (i.e., J_z) can be obtained from the horizontal magnetic field components (i.e., B_x and B_y), using Ampere's law (Kontogiannis et al. 2017;

Fleishman & Pevtsov 2018; Fursyak et al. 2020):

$$J_z = \frac{1}{\mu_0}\left(\frac{dB_y}{dB_x} - \frac{dB_x}{dB_y}\right). \tag{1}$$

The magnetic field components (B_z, $-B_y$, B_x) in heliographic Cartesian coordinates can be approximately obtained from the corresponding field components (B_r, B_θ, B_ϕ) in heliocentric spherical coordinates (Gary & Hagyard 1990). In order to calculate the longitudinal current (I_z) from the longitudinal current density (J_z), we need to multiply J_z by the area of one pixel, i.e., 13.14×10^{10} m^2. In Figure 11, we present the distribution of the current (i.e., I_z), along with the structure of the radial component of the magnetic field (i.e., B_r), within the FR, before the start of the flares. The top, middle, and bottom panels of Figure 11 correspond to F1, F2, and F3, respectively. For better visualizations, we saturate the current values at $\pm 0.5 \times 10^{10}$ A in all panels. The color code for the I_z maps (Figures 11(a), (c), and (e)) is shown by a colorbar in Figure 11(a). We observe a significant amount of current concentration along the western PIL (see the sky blue dotted lines in Figures 9(e), (g), and (k)) of the FR for all events. Notably, the negative current largely dominates the positive current in all cases. Between F2 and F3, the western PIL undergoes elongation (Figure 11(f); see also Figures 9(k) to (m)). In a similar way, the region of strong photospheric currents that predominantly exists at the flaring core region is
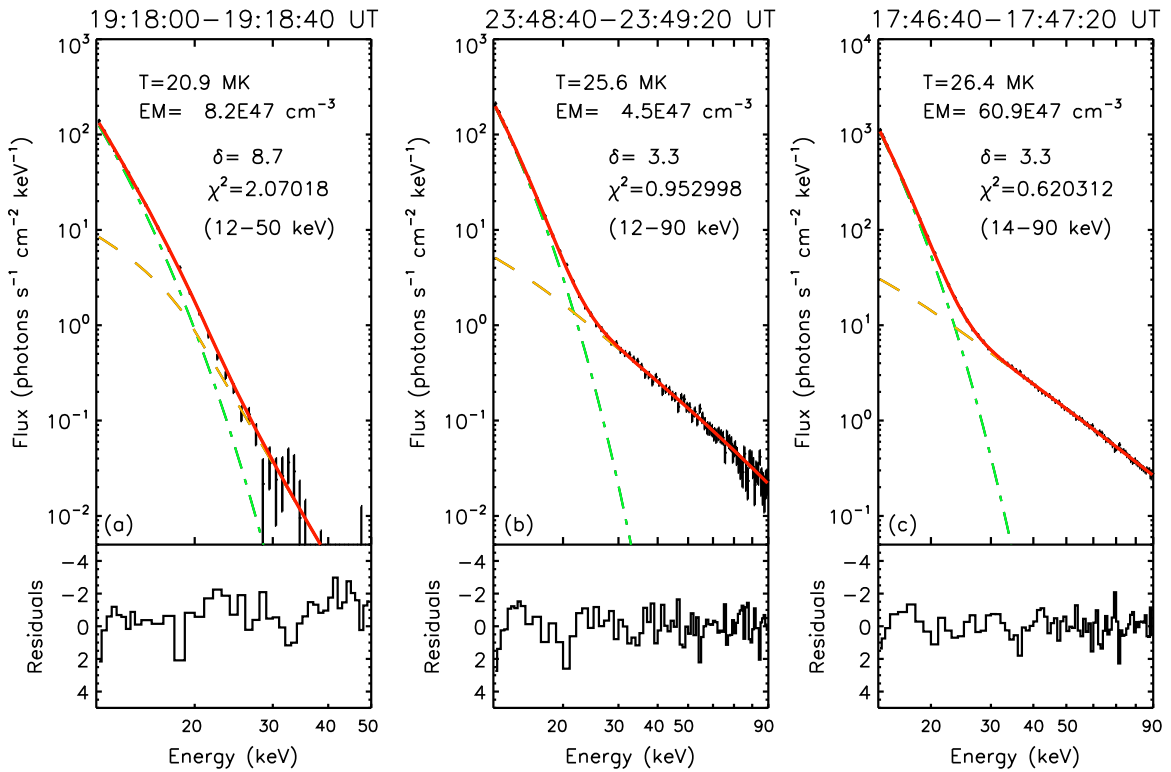
Figure 8. Results of the RHESSI X-ray spectral fit, along with their residuals, for all the events under analysis. We use an isothermal model (shown by the green dashed–dotted line) for the thermal fit and a thick-target Bremsstrahlung model (shown by the yellow dashed line) for nonthermal fit of the observed spectra. The solid red line indicates the sum of the two components. Each spectrum was accumulated with an integration time of 40 s, using the front segments of detectors 1–9 (except for detectors 2 and 7). The energy ranges that we select for the spectral fit are annotated in the respective panels. In (a), (b), and (c), we show the spectra at the peak of the HXR emissions during the M2.0, M2.6, and X1.0 flares, respectively.

observed to show an extended morphological structure prior to F3 (see Figures 11(a), (c), and (e)).

6. Onset of Eruption

For a quantitative understanding of the eruption from the flaring core, we present time slice diagrams in Figure 12. Figures 12(a)–(b), (c)–(d), and (e)–(f) correspond to F1, F2, and F3, respectively. In the left column of this figure, we show the directions of the slits along which we observe significant eruptive features. In the right column, we show the corresponding time slice diagrams in AIA 94 Å running difference images, constructed by tracking the eruptive signatures along the slits. We mark the erupting hot plasma structures with the red dots in Figures 12(b), (d), and (f). We note that the speeds of the hot plasma ejections show an increasing trend from F1 to F3 (i.e., ≈296, 581, and 955 km s^{-1}). Following the hot plasma eruption, an eruption of dark (i.e., cool) material ensues, which we indicate with the white arrows. To compare the eruption of the plasma structure with the temporal evolution of the flare, we overplot the AIA 94 Å flare light curves in all panels. We note that the rise of the 94 Å intensity is near simultaneous with the onset of the hot plasma eruption from the flaring core. Subsequently, the eruptions from the source region turn into CMEs. According to the Large Angle and Spectromeric Coronagraph Experiment (LASCO) CME catalog,[8] the linear speeds of the CMEs within the LASCO field of view (FOV)

that are associated with F1, F2, and F3 are 420, 503, and 528 km s^{-1}, respectively.

7. Evolution of Free Magnetic Energy

Our analysis is comprised of homologous eruptive flares, which show gradually increasing SXR intensities (M2.0, M2.6, and X1.0). To investigate the scenario in the framework of the storage and release process of the free magnetic energy associated with the complex magnetic configuration of the AR, we calculate the temporal evolution of the free energy over an interval of ≈30 hr, which is demonstrated in Figure 13. The free magnetic energy (E_F) is defined as the difference between the nonpotential (E_{NP}) and potential (E_P) magnetic energies, i.e.:

$$E_F = E_{NP} - E_P, \qquad (2)$$

where E_{NP} is calculated from the magnetic fields obtained from the NLFFF extrapolation. The different forms of energies can be calculated from the magnetic field information using the following relation:

$$E = \int_V \frac{B^2}{8\pi} \, dV. \qquad (3)$$

We observe that there is a prominent decrease of the free magnetic energy due to the occurrence of the flaring events. We calculate the decreases to be 17%, 9.5%, and 38% for the events M2.0, M2.6, and X1.0, respectively. There is a data gap in the GOES light curve (in the 1–8 Å channel) from 08:30 UT to 09:40 UT on 2014 March 29, which is indicated by the hatched region. To confirm whether the GOES SXR flux
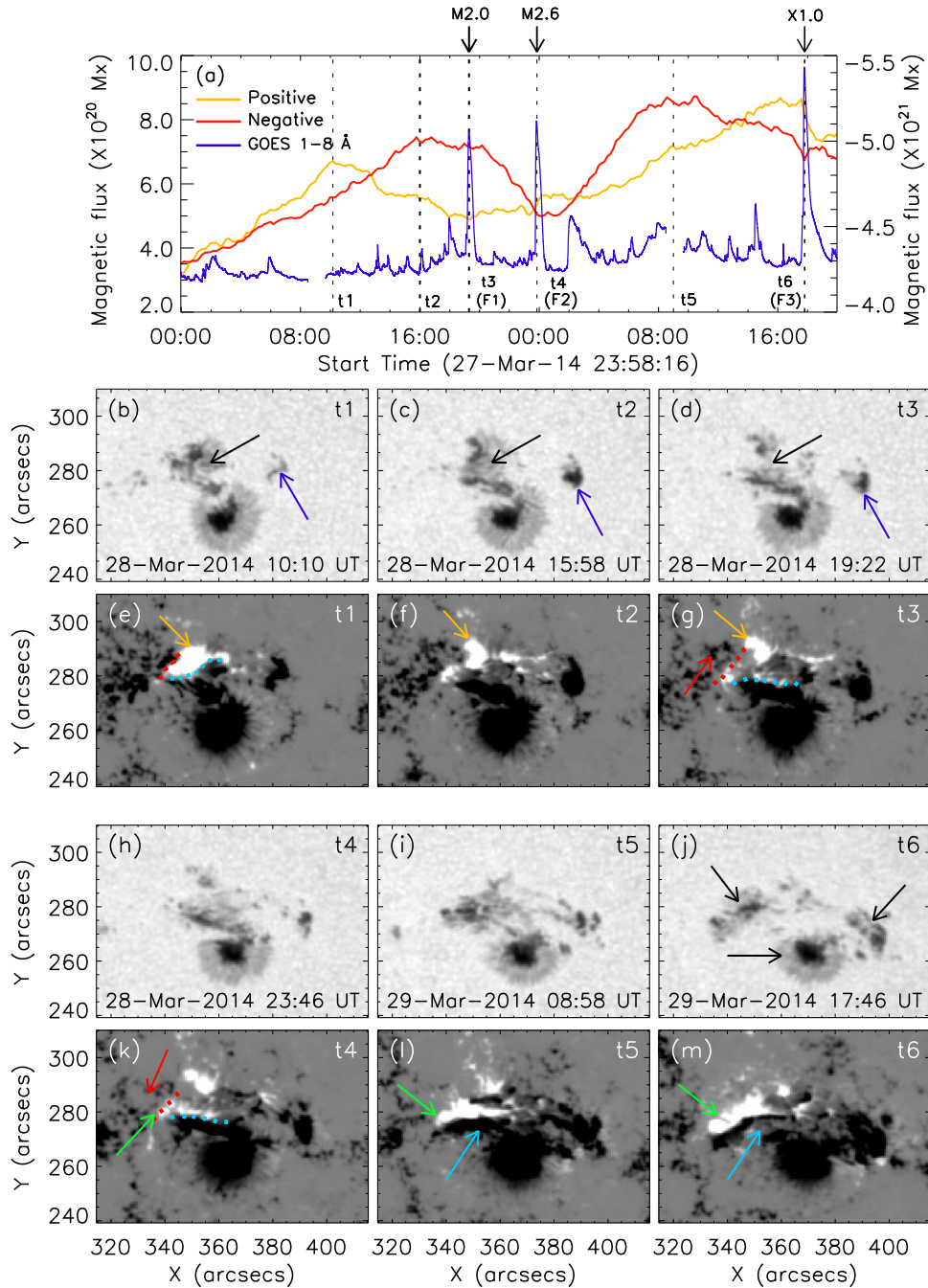
Figure 9. (a) The temporal evolution of the magnetic flux obtained from the FR, along with the GOES SXR light curve in the 1–8 Å channel. (b)–(d) Intensity images of the FR at three instances—$t1$, $t2$, and $t3$—as marked in (a). The black arrows denote small-scale changes in the northern sunspot group, while the blue arrows indicate the growth of a compact sunspot group. (e)–(g) LOS magnetogram images that are cotemporal with the continuum observations (shown in the row above) at times $t1$, $t2$, and $t3$, respectively. The yellow and red arrows are used to indicate the changes in the positive and negative fluxes, respectively. (h)–(j) Intensity images of the FR at $t4$, $t5$, and $t6$, as marked in (a). The arrows in panel (j) indicate three distinct sunspot groups. (k)–(m) LOS magnetogram images for $t4$, $t5$, and $t6$ that are cotemporal with the corresponding continuum observations (shown in the row above). The yellow (see panels (e)–(g)) and red (see panels (g) and (k)) arrows are used to indicate the changes in the positive and negative fluxes, respectively. The green and sky blue arrows are used to indicate the changes in positive and negative fluxes, respectively. The red and sky blue dotted lines in (e), (g), and (k) denote the PILs in the eastern and western parts of the FR, respectively. An animation representing the continuum (top panel) and LOS magnetogram (bottom panel) observations of the AR is available in the online material. It runs from 00:00 UT on 2014 March 28 to 20:00 UT on 2014 March 29. The region marked by the black and white boxes in the top and bottom panels of the animation represents the FR (see Figure 2).

(An animation of this figure is available.)

enhancements are associated with the flaring activity in AR 12017, in which we are interested, we have shown the AIA 94 Å light curve deduced exclusively from the AR. It is observed that, in general, the EUV light curve matches well with the GOES light curve, and the prominent SXR peaks represent the activity in the AR.

8. Discussion

In this study, we explore the multiwavelength evolution of three homologous flaring events of successively increasing intensities and their associated energy release processes. The events occurred between 2014 March 28 and 29, in NOAA AR
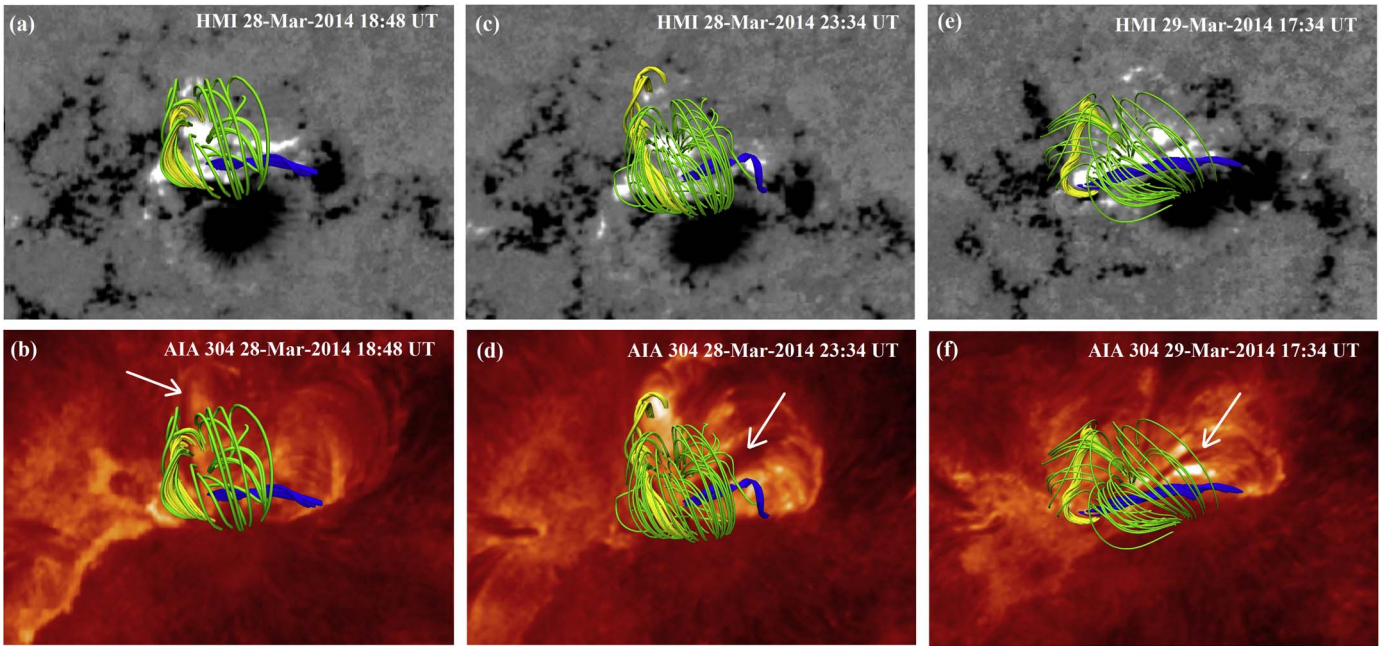
Figure 10. The preflare coronal magnetic structures obtained through NLFFF modeling, presented over the photospheric radial magnetic fields (top) and the AIA 304 Å observations (bottom), in and around the FR for all the events. (a)–(b), (c)–(d), and (e)–(f) denote the epochs corresponding to F1, F2, and F3, respectively. We note the existence of two flux ropes, shown by the yellow and blue field lines, residing over the eastern and western PILs of the FR (top panels; see also Figure 9), respectively. The flux ropes are enveloped by the low-lying bipolar field lines (green). In the bottom panels, we mark the filaments with arrows, observed through EUV imaging.

12017, over an interval of ≈24 hr. The flares were triggered by eruptions of flux ropes from the core of the AR. The importance of this study lies in its investigation of the intrinsic coupling of magnetic fields and associated processes, from the photosphere to the corona, which resulted in the repetitive buildup of compact magnetic flux ropes and their subsequent eruptions, observed in the form of homologous eruptive flares of successively increasing intensities. The important observational aspects of this study are summarized as follows:

1. According to the GOES observations, the durations of the flares of our analysis are 22, 14, and 19 minutes, for the M2.0 (F1), M2.6 (F2), and X1.0 (F3) flares, respectively (see Table 1). A statistical analysis of almost 50,000 GOES SXR flares over the period from 1976 to 2000 is presented in Veronig et al. (2002). Their analysis reveals that the average values of the durations of M- and X-class flares are 24 and 30 minutes, respectively. In view of this, the duration of F1 is close to the value as suggested by the study of Veronig et al. (2002), while F2 and F3 have shorter durations. Notably, although F1 and F2 are of comparable intensity, and are homologous in nature, the duration of F2 is significantly shorter than that of F1. On the other hand, F3, despite being a large X-class flare, exhibits a shorter duration as compared to F1.

2. The inspection of the RHESSI X-ray images in multiple energy bands within the energy range 3–100 keV during the evolution of F1 and F2 reveals a single X-ray source persisting throughout the flaring intervals. In both events, the X-ray emissions are observed to come from the dense and closely packed coronal loop system. The X-ray observations during the third event reveal emissions from different spatial locations within the FR (see Figure 6). During the onset of the impulsive phase of the third flare, we observe X-ray emissions from both the eastern and western parts of the FR (Figures 6(d) and (e)). Notably, conjugate X-ray sources with two distinct centroids in the 50–100 keV energy range are observed within the core region during the peak of the X1.0 flare (Figure 6(f)). These conjugate X-ray sources likely originate from the deposition of energy by energetic electrons at the footpoints of the post-reconnected loop system, as depicted in the standard flare model (see, e.g., Joshi et al. 2009).

3. We observe significant cancellations of magnetic fluxes (both positive and negative) within a bipolar flaring core region, near the eastern and western PILs (see Figure 9 and Section 4.1). A detailed comparison of the HMI magnetograms and EUV images (see Figures 3–7 and Figure 9) reveals that the source region of the eruptions is spatially well correlated with the compact PILs (see Figure 10). Notably, we observe significant flux changes near the eastern PIL before F1 and F2, whereas the change of flux is at its maximum near the western PIL before F3 (see Figure 9). Thus, our observations imply a precise link between each flux rope eruption and magnetic flux cancellation in the photosphere. The observations of extended phases of flux cancellation, together with the prominent flux canceling features near the PIL, have important implications for understanding the repetitive buildup of the flux ropes and the triggering mechanism of the homologous eruptions. Contextually, from the EUV imaging observations, we note that the eruptions were initiated from the eastern PIL, during F1 and F2, whereas during F3, the eruption was triggered from the western PIL. These observations show conformity with the tether-cutting model of solar eruption (Moore & Roumeliotis 1992; Moore et al. 2001), where the buildup process of a flux rope along the PIL is
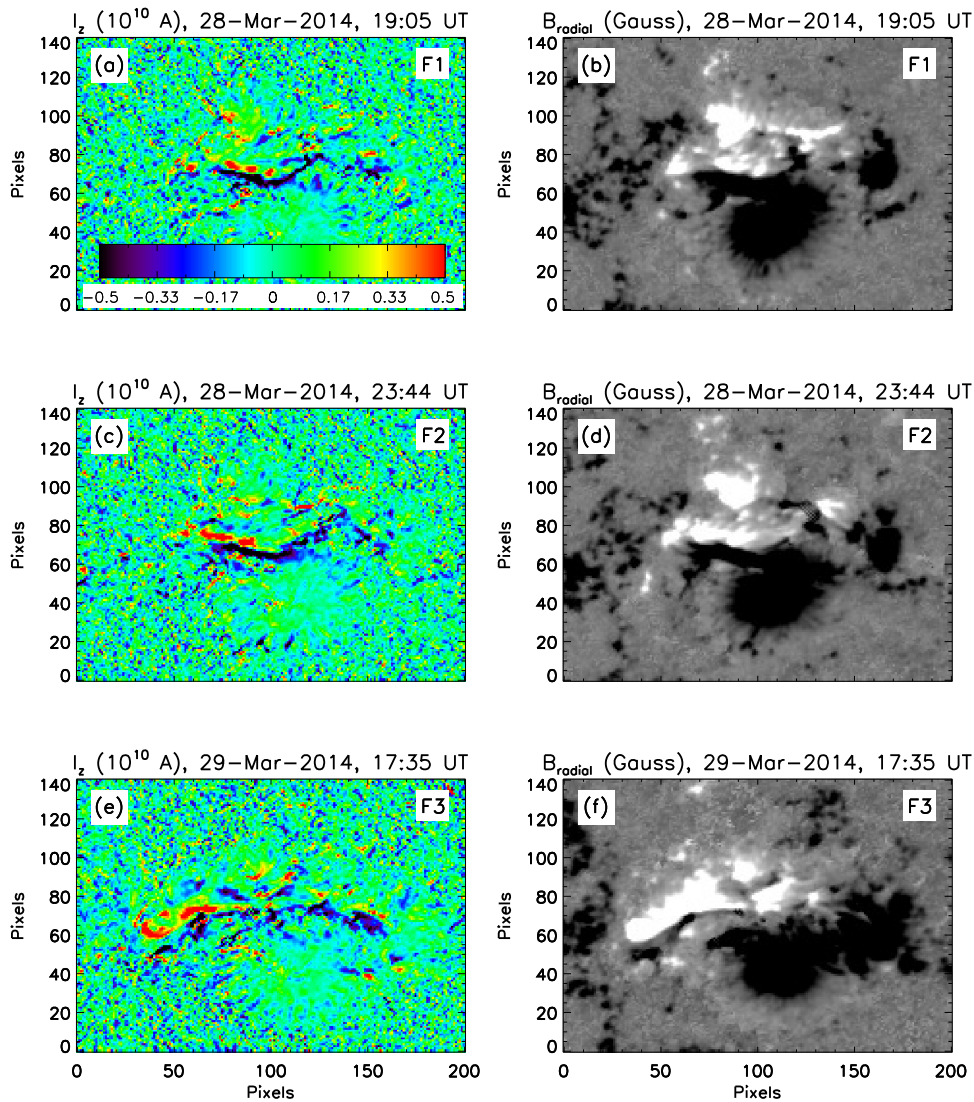
Figure 11. Comparisons of the photospheric longitudinal current (I_z; first column) and the radial component of the magnetic field (B_{radial}; second column) before the onset of the flares. (a)–(b), (c)–(d), and (e)–(f) correspond to F1, F2, and F3, respectively. In (a), we denote a colorbar corresponding to the distribution of I_z in (a), (c), and (e). We saturate the I_z and B_{radial} values to $\pm 0.5 \times 10^{10}$ A and ± 500 G, respectively, in all panels. We note that the current distribution is strong near the western PIL of the FR (see Figure 9), and that it elongates along the PIL before F3. The morphological changes in the longitudinal current distribution are similar to the structural changes in the distribution of the radial magnetic field component (see (e) and (f)).

governed by flux cancellation, which extends over a much longer interval as compared to the flare timescales. The preexistence of magnetic flux ropes in ARs in relation to eruptive flares and CMEs has been well recognized (see, e.g., Shibata 1999). Several contemporary observations have also confirmed the slow activation of a magnetic flux rope, prior to the flare's impulsive phase (e.g., Joshi et al. 2016; Mitra & Joshi 2019; Sahu et al. 2020; Kharayat et al. 2021). In our work, for each eruption, the NLFFF extrapolation results reveal the presence of two flux ropes, corresponding to the eastern and western PILs. The synthesis of EUV imaging, magnetogram observations, and NLFFF modeling suggests that the formed flux rope was likely destabilized by rapidly evolving localized magnetic field structures near the PIL, indicating the role of small-scale tether-cutting reconnection in the triggering process. This scenario is further confirmed by the location of the X-ray sources during the early phase, when the emission only originates

at lower energies (below 25 keV; see Figures 3(b), 5(c), and 6(b)), as these sources are well correlated with the locations of prominent flux cancellation.

4. We further highlight the results of NLFFF extrapolation, which reveal the presence of two magnetic flux ropes, formed over the eastern and western PILs, prior to each eruptive flare. In this context, it is relevant to discuss and compare the different aspects relating to the magnetic flux rope manifestations in this AR, as studied in detail by Yang et al. (2016) and Woods et al. (2018), in association with the flaring activity of March 28–29. Using an NLFFF model, Yang et al. (2016) showed a magnetic flux rope in the region, for which the twist number and decay index of the constraining field were calculated. Their analysis revealed that the decay index lies below the critical value for torus instability to be operational. Therefore, the authors favored the role of twist instability toward the CME onset, although they could not find a common critical value for the twist number over which
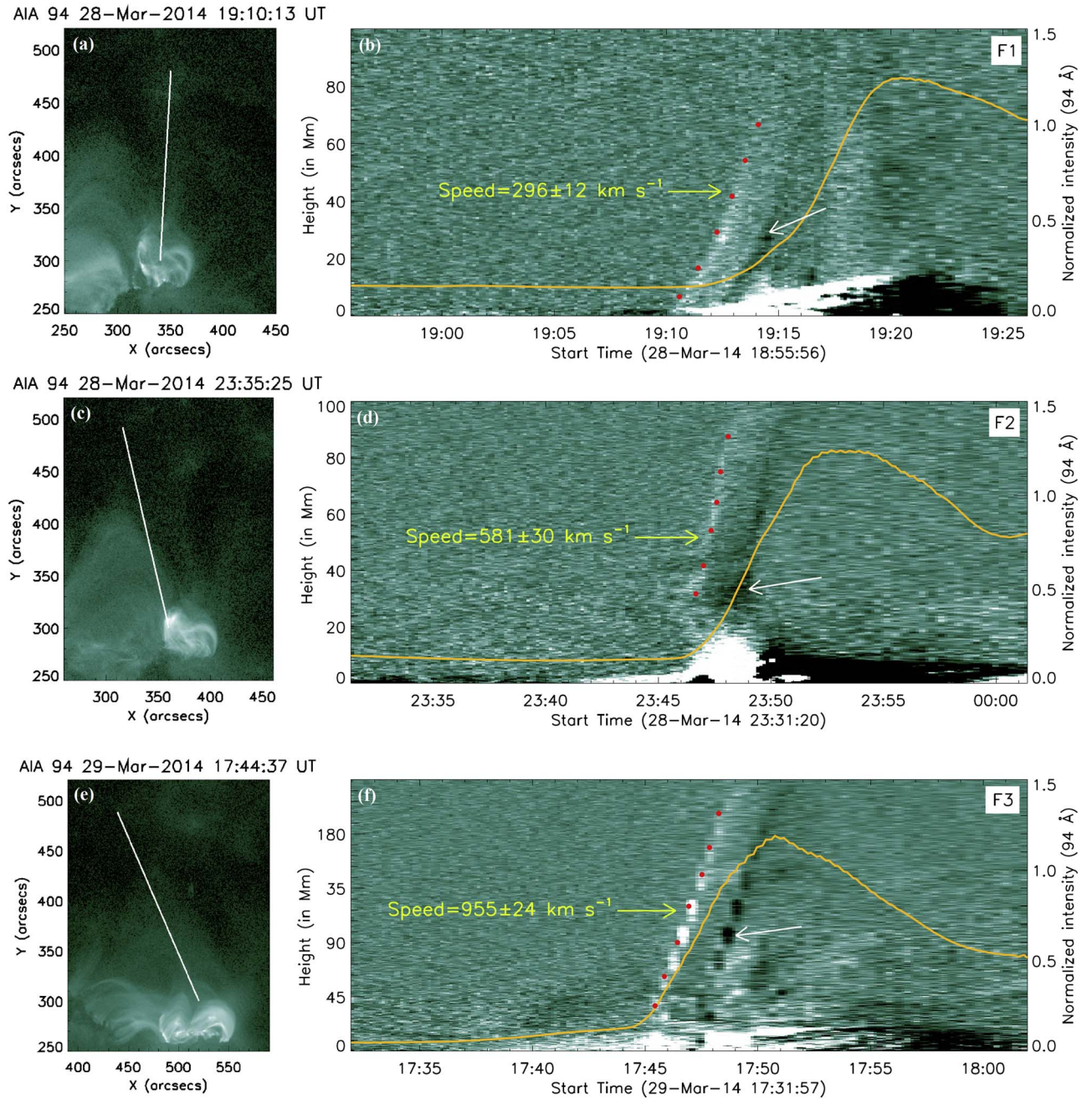
Figure 12. The evolutionary stages of the eruption of the hot plasma structures from the core FR. (a)–(b), (c)–(d), and (e)–(f) correspond to F1, F2, and F3, respectively. The left column shows the directions of the slits over the AIA 94 Å direct images along which we calculate the height–time profiles of the eruptions. In the right column, we show time slice diagrams obtained from the AIA 94 Å running difference images, by tracking the intensity variation along the slits. The erupting hot plasma structures are indicated by the red dots in (b), (d), and (f). The speeds of the erupting structures are annotated in these panels, with the corresponding uncertainties in the measurements. We note that the speeds gradually increase from F1 to F3. Following the hot plasma eruption, we observe the eruption of a dark (i.e., cool) structure, which we mark with the white arrows in these panels. The flare intensity profiles in the AIA 94 Å channel are also overplotted with the orange curves.

the flux rope tends to erupt. Nevertheless, their work points toward the fact that the twist number is a sensitive parameter in relation to flare occurrence. In a subsequent work, Woods et al. (2018) studied the most energetic flare (the X1.0 event) from this AR, which is the third event in our study. They found that the flux rope actually comprised two flux ropes, only one of which erupted during the X1.0 flare. The detailed EUV and X-ray imaging observations presented in our work also reveal the destabilization of the flux rope formed at the western

PIL, in agreement with the work of Woods et al. (2018). Due to the presence of the magnetic flux cancellation and the brightening below the flux rope, Woods et al. (2018) concluded that the tether-cutting mechanism was responsible for the rising of the western flux rope to a torus unstable region prior to the flare. From the flare light curves, together with the corresponding EUV imaging observations, we clearly find preflare brightening for the X1.0 flare (see Figures 6(a) to (d)), which further points toward the role of tether-cutting reconnection for the
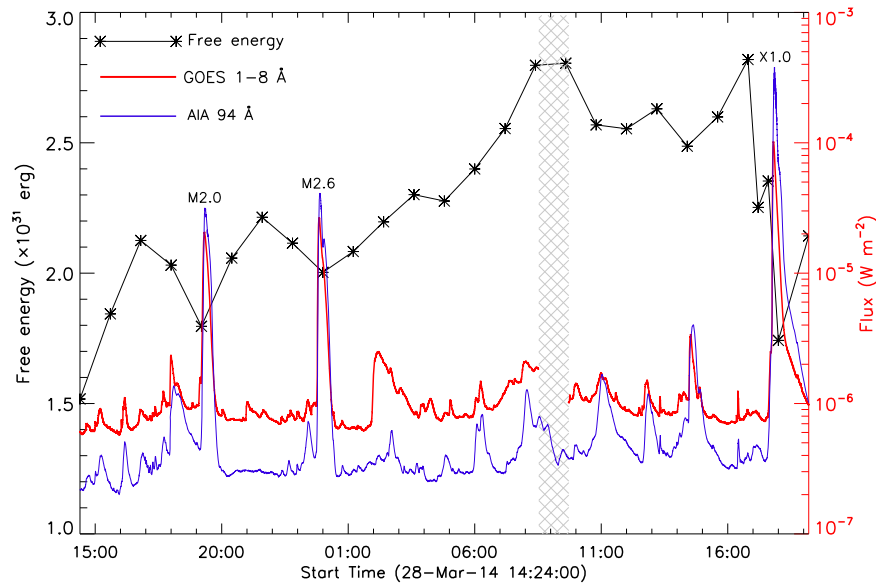
Figure 13. The evolution of the free magnetic energy over an interval of ≈30 hr, encompassing all the flares in the study. The free energy was calculated for the coronal volume encompassing the AR, taking the HMI SHARP CEA cutout as the photospheric boundary. We also plot the full-disk GOES light curve in the 1–8 Å channel. The hatched region shows an interval during which the GOES data are not available. To complement the data gap, we plot an EUV 94 Å intensity curve, obtained from AIA, recorded for the AR.

activation of the flux rope to the torus unstable region. For a series of four eruptive events, similar results were obtained by Mitra & Joshi (2021), who proposed the combined roles of ideal (torus) and resistive (tether-cutting) instability for the onsets of CMEs.

5. The sequential eruptions of the flux ropes from the flaring core give rise to corresponding CMEs. The inspection of the series of AIA 94 Å running difference images reveals eruptions of hot coherent plasma structures (i.e., heated flux ropes) from the core region (Figure 12). We note that the speeds of the flux rope eruptions in the source region significantly increase from F1 to F3. A comparison of the speeds of the eruptive flux ropes at the source region with the corresponding CMEs in the LASCO FOV (see Section 6) reveals that the first flux rope undergoes acceleration (296 versus 420 km s^{-1}), the second one moves with approximately constant speed (581 versus 503 km s^{-1}), while the final eruption exhibits deceleration (955 versus 528 km s^{-1}).

6. The buildup of the electric current in the photosphere is directly associated with the emergence of current-carrying flux (Tan et al. 2006; Török et al. 2014). The photospheric currents prior to the flare onset signify the buildup of nonpotentiality in the AR corona (Schrijver et al. 2005; Dalmasse et al. 2015). Our study reveals that a strong current accumulation occurs near the western PIL of the FR (Figure 11), where one of the two flux ropes lies (Figure 10). Furthermore, before F3, the magnetic flux near the western PIL is observed to undergo expansion, showing an extended morphology (Figure 11(f)). In response to this, the longitudinal current distribution is elongated along the same PIL before F3 (Figure 11(e)). In general, photospheric currents have important consequences in terms of triggering solar eruptive events. Mitra et al. (2020a) studied the role of precursor flare activity in triggering a dual-peak M-class flare. Their study revealed the presence of strong localized regions of photospheric currents of opposite polarities at the precursor location, making the region susceptible to small-scale magnetic reconnection.

7. The photospheric flux emergence and shearing motion introduce strong electric currents and inject energy into the AR corona. The coronal fields is reconfigured in this process, resulting in the accumulation of free magnetic energy in the coronal volume (Régnier 2012; Vekstein 2016). This stored free energy is regarded as a prime factor that is responsible for the explosive phenomena. The successively increasing intensities of the homologous flares of our analysis point toward a complex "storage and release" process of magnetic energies in the AR. For a quantitative understanding of the energy storage and release process, we study the evolution of the free magnetic energy over a time span covering the three homologous events (Figure 13). We find that the maximum release of the free magnetic energy (i.e., 38%) is observed during the strongest event (i.e., the F3/X1.0 flare). It is also remarkable to observe that the third event has a prolonged period for the storage of the free magnetic energy (i.e., a period of ≈ 17 hr between F2 and F3), during which no major flare above class C occurs in the AR. Interestingly, this "storage phase" largely overlaps with a persistent phase of flux emergence (see Figure 9(a); the interval between $t4$ and $t5$). In conclusion, our analysis reveals that the dominant variation in the magnetic flux (both at a large scale, involving the full FR, as well as at small scales, close to the compact PILs) and the buildup of free magnetic energy in and around the FR is the root cause for the homologous eruptive flares of successively increasing intensities.

In summary, our paper provides a detailed investigation of the multiwavelength evolutions of three homologous eruptive flares, by combining HXR, EUV, white-light, and magnetogram observations. We provide a quantitative estimation of the evolution of the free magnetic energy in the corona associated

with the AR, and we explore its links with the ongoing photospheric and coronal processes. Thus, our study brings out the connection between the photospheric developments and the resulting rapid buildup and subsequent eruption of coronal magnetic structures.

ORCID iDs

Suraj Sahu https://orcid.org/0000-0001-8377-8640
Bhuwan Joshi https://orcid.org/0000-0001-5042-2170
Avijeet Prasad https://orcid.org/0000-0003-0819-464X
Kyung-Suk Cho https://orcid.org/0000-0003-2161-9606

References

Benz, A. O. 2017, LRSP, 14, 2
Chatterjee, P., & Fan, Y. 2013, ApJL, 778, L8
Cheung, M. C. M., Rempel, M., Chintzoglou, G., et al. 2019, NatAs, 3, 160
Dalmasse, K., Aulanier, G., Demoulin, P., et al. 2015, ApJ, 810, 17
DeVore, C. R., & Antiochos, S. K. 2008, ApJ, 680, 740
Fleishman, G. D., & Pevtsov, A. A. 2018, in Electric Currents in Geospace and Beyond, ed. A. Keiling, O. Marghitu, & M. Wheatland, Vol. 235 (Washington, DC: American Geophysical Union), 43
Fletcher, L., Dennis, B. R., Hudson, H. S., et al. 2011, SSRv, 159, 19
Fursyak, Y. A., Kutsenko, A. S., & Abramenko, V. I. 2020, SoPh, 295, 19
Gary, G. A., & Hagyard, M. J. 1990, SoPh, 126, 21
Holman, G. D., Sui, L., Schwartz, R. A., & Emslie, A. G. 2003, ApJL, 595, L97
Hurford, G. J., Schmahl, E. J., Schwartz, R. A., et al. 2002, SoPh, 210, 61
Joshi, B., Ibrahim, M. S., Shanmugaraju, A., & Chakrabarty, D. 2018, SoPh, 293, 107
Joshi, B., Kushwaha, U., Veronig, A. M., & Cho, K.-S. 2016, ApJ, 832, 130
Joshi, B., Veronig, A., Cho, K.-S., et al. 2009, ApJ, 706, 1438
Kharayat, H., Joshi, B., Mitra, P. K., Manoharan, P. K., & Monstein, C. 2021, SoPh, 296, 99
Kleint, L., Battaglia, M., Reardon, K., et al. 2015, ApJ, 806, 9
Kontogiannis, I., Georgoulis, M. K., Park, S.-H., & Guerra, J. A. 2017, SoPh, 292, 159
Lemen, J. R., Title, A. M., Akin, D. J., et al. 2012, SoPh, 275, 17
Li, S., Jaroszynski, S., Pearse, S., Orf, L., & Clyne, J. 2019, Atmos, 10, 488
Li, Y., Ding, M. D., Qiu, J., & Cheng, J. X. 2015, ApJ, 811, 7
Li, Y., Lynch, B. J., Welsch, B. T., et al. 2010, SoPh, 264, 149
Lin, R. P., Dennis, B. R., Hurford, G. J., et al. 2002, SoPh, 210, 3
Liu, C., Deng, N., Liu, R., et al. 2015, ApJL, 812, L19
Mitra, P. K., & Joshi, B. 2019, ApJ, 884, 46
Mitra, P. K., & Joshi, B. 2021, MNRAS, 503, 1017
Mitra, P. K., Joshi, B., & Prasad, A. 2020a, SoPh, 295, 29
Mitra, P. K., Joshi, B., Prasad, A., Veronig, A. M., & Bhattacharyya, R. 2018, ApJ, 869, 69
Mitra, P. K., Joshi, B., Veronig, A. M., et al. 2020b, ApJ, 900, 23
Moore, R. L., & Roumeliotis, G. 1992, in Triggering of Eruptive Flares—Destabilization of the Preflare Magnetic Field Configuration, ed. Z. Svestka, B. V. Jackson, & M. E. Machado, Vol. 399 (New York: Springer), 69
Moore, R. L., Sterling, A. C., Hudson, H. S., & Lemen, J. R. 2001, ApJ, 552, 833
Nitta, N. V., & Hudson, H. S. 2001, GeoRL, 28, 3801
Pesnell, W. D., Thompson, B. J., & Chamberlin, P. C. 2012, SoPh, 275, 3
Priest, E. R., & Forbes, T. G. 2002, A&ARv, 10, 313
Régnier, S. 2012, SoPh, 277, 131
Romano, P., Elmhamdi, A., Falco, M., et al. 2018, ApJL, 852, L10
Romano, P., Zuccarello, F., Guglielmino, S. L., et al. 2015, A&A, 582, A55
Sahu, S., joshi, B., Mitra, P. K., Veronig, A. M., & Yurchyshyn, V. 2020, ApJ, 897, 157
Sahu, S., Joshi, B., Sterling, A. C., Mitra, P. K., & Moore, R. L. 2022, ApJ, 930, 41
Schou, J., Scherrer, P. H., Bush, R. I., et al. 2012, SoPh, 275, 229
Schrijver, C. J., DeRosa, M. L., Title, A. M., & Metcalf, T. R. 2005, ApJ, 628, 501
Shibata, K. 1999, Ap&SS, 264, 129
Smith, D. M., Lin, R. P., Turin, P., et al. 2002, SoPh, 210, 33
Tan, B., Ji, H., Huang, G., et al. 2006, SoPh, 239, 137
Toriumi, S., & Wang, H. 2019, LRSP, 16, 3
Török, T., Leake, J. E., Titov, V. S., et al. 2014, ApJL, 782, L10
Vekstein, G. 2016, JPlPh, 82, 925820401
Vemareddy, P. 2017, ApJ, 845, 59
Veronig, A., Temmer, M., Hanslmeier, A., Otruba, W., & Messerotti, M. 2002, A&A, 382, 1070
Wiegelmann, T. 2008, JGRA, 113, A03S02
Wiegelmann, T., & Inhester, B. 2010, A&A, 516, A107
Wiegelmann, T., Thalmann, J. K., Inhester, B., et al. 2012, SoPh, 281, 37
Woodgate, B. E., Martres, M.-J., Smith, J. B., Jr., et al. 1984, AdSpR, 4, 11
Woods, M. M., Harra, L. K., Matthews, S. A., et al. 2017, SoPh, 292, 38
Woods, M. M., Inoue, S., Harra, L. K., et al. 2018, ApJ, 860, 163
Yang, K., Guo, Y., & Ding, M. D. 2016, ApJ, 824, 148
Young, P. R., Tian, H., & Jaeggli, S. 2015, ApJ, 799, 218
Zhang, J., & Wang, J. 2002, ApJL, 566, L117
Zuccarello, F., Ermolli, I., Korsos, M. B., et al. 2021, RAA, 21, 313